Quasar Mesolensing - Direct Probe to Substructures around Galaxies -

Atsunori YONEHARA*

Center for Computational Physics, University of Tsukuba,
Tennoudai 1-1-1, Tsukuba, Ibaraki, 305-8577, JAPAN
yonehara@rccp.tsukuba.ac.jp

Masayuki UMEMURA

Center for Computational Physics, University of Tsukuba,
Tennoudai 1-1-1, Tsukuba, Ibaraki, 305-8577, JAPAN
umemura@rccp.tsukuba.ac.jp

and

Hajime SUSA

Institute of Theoretical Physics, Rikkyo University,
Nishi-Ikebukuro 3-34-1, Toshima-ku, Tokyo, 171-8501, JAPAN
susa@rikkyo.ne.jp

Abstract

Recently, "CDM crisis" is under discussion. The main point of this crisis is that number of substructures presented by cosmological N-body simulations based on CDM scenario for structure formation is much larger than observed substructures. Therefore, it is crucial for this crisis to discriminate whether expected number of CDM substructures really exist but non-luminous or do not exist.

In this paper, we present a new idea to detect such invisible substructures by utilizing a gravitational lensing. Here, we consider quasars that are gravitationally lensed by a foreground galaxy. A substructure around the lensing galaxy may superposed on one of the lensed images of such quasars. In this situation, additional image splitting should occur in the image behind the substructure, and further multiple images are created. This is "quasar mesolensing".

We estimate separation and time delay between further multiple images due to quasar mesolensing. The expected value is $1 \sim 30$ milli-arcsecond for the separation and future fine resolution imaging enable us to find invisible substructures, and is $1 \sim 10^3$ second for the time delay and high-speed monitoring of such quasar will be able to find "echo"-like variation due to quasar mesolensing in intrinsic variability of the quasar. Furthermore, we evaluate that the optical depth for the quasar mesolensing

arXiv:astro-ph/0310296v1 10 Oct 2003

is ~ 0.1. Consequently, if we monitor a few multiple quasars, we can find "echo"-like variation in one of the images after intrinsic flux variations of quasars.

Key words: galaxies: formation, galaxies: structure, gravitational lensing

1. Introduction

Cold Dark Matter (CDM) scenario for structure formation have been widely accepted in our Universe, and WMAP results (Spergel et al. 2003) also strengthened this scenario. In addition, numerical simulations for structure formation based on CDM scenario nicely reproduce observed, large scale structures such as cluster of galaxies. However, as recently mentioned by Klypin et al. (1999) and Moore et al. (1999), the scenario meets crisis in small scale structures. In their high resolution, cosmological N-body simulation based on CDM scenario, there are too many "subhalos (or substructures)" around galactic scale objects compared with actually observed substructures around Milky Way. If CDM scenario for structure formation is correct, many substructures should be invisible or not detectable due to very low star formation efficiency by some feedback processes (e.g., Nishi & Susa 1999; Kitayama et al. 2001 or Susa & Umemura 2003) at least in current observational instruments. However, how can we confirm or reject the existence of theoretically predicted, many number of substructures around galaxies ? The best probe can be gravitational lensing, since not brightness or luminosity of objects but only mass or density profile of objects is essential to this phenomenon. Thus, we may be able to probe invisible substructures around galaxies by utilizing gravitational lensing.

Recently, Chiba (2002) extends arguments of Mao & Schneider (1998) and presents a nice idea. He focused on magnification anomalies in multiple images of two gravitationally lensed quasars. Such anomalies cannot be explained by smooth single lens model for lens galaxies and he proposed that the possible explanation for such flux anomalies is the existence of substructures around lens galaxies. Following this work, Dalal & Kochanek (2002) investigate satellite mass fraction for seven gravitationally lensed quasars via Monte Carlo simulations, and they find that the resultant satellite mass fraction, ~ 10 % agree with predictions of cosmological N-body simulation based on CDM scenario (see also Metcalf & Madau 2001, Metcalf & Zhao 2002). Furthermore, Metcalf & Madau (2001) and Metcalf (2002) mentioned that milliarcsecond scale bending of radio jets in gravitationally lensed quasar is due to the distortion by gravitational lens effect of substructures around the lens galaxy.

These works seem to find a way to save CDM scenario for structure formation from its crisis, but there still remains some ambiguity. First of all, flux magnification due to gravitational lens effect does not directly reflect mass of the lens, and magnification anomalies may not be direct evidence for substructures around lens galaxies. For example, as is well known in

gravitationally lensed quasar with quadruple image, Q2237+0305 (Huchra's Lens or Einstein Cross), gravitationally lensed quasars may suffer quasar microlensing by stellar mass objects in the lens galaxy (Østensen et al. 1996, see also Østensen et al. 1997, Jackson, Xanthopoulos & Browne 2000, Gil-Merino, Wisotzki & Wambsganss 2002, Oshima et al. 2001 for quasar microlensing in another system). Thus, magnification anomalies due to quasar microlensing can be occurring in most of gravitationally lensed quasars [1]. However, the time scales for such phenomena in most systems are quite long compared with Q2237+0305, say several years, due to long distance to the lens galaxy, and it is difficult to discriminate magnification anomalies due to substructures around galaxies and that due to quasar microlensing only a few photometric observation. Secondly, image distortion of radio jets seems to stronger evidence for substructures around galaxies, but it can still not be direct evidence for such structures. The reason is the structure of radio jets is generally complicated and it may not easy task to find distortion between radio jets in corresponding images. Of course, different from magnification, image distortion can be an indicator for typical scale of gravitational lens, e.g., Einstein ring radius, and also for mass of the lens. However, the proposed idea is based on weak lensing regime, and it is not clear that the scale of distortion directly reflects the scale of gravitational lens, and there still remains some ambiguity, too.

In this paper, we investigate new important aspects of gravitational lensing to obtain more direct evidence for substructure around galaxies than previously proposed ideas. Here, we focus on strong lensing regime of gravitational lens effects by substructures. In this regime, further multiple images in one of multiple images of gravitationally lensed quasars are expected. This interesting phenomenon has never been discussed before, and we estimate expected values for the image separation and the time delay between such further multiple images. Reflecting mass of the lens objects, the values should be smaller than those for macrolensing due to galactic scale lens, but larger than those for microlensing due to stellar scale lens, and this gravitational lens effect can be called "quasar mesolensing". Different from magnification anomaly, image separation and time delay between further multiple images induced by quasar mesolensing directly reflect mass of the lens objects via typical lens size such as Einstein ring radius for point mass lens, and these signals can be stronger evidences for the existence of substructures than magnification anomaly. In next section, we show that gravitationally lensed quasars are the most suitable targets to probe substructures around galaxies from simple argument. In section 3, lens models and numerical method are investigated, and the results of our calculations are presented in section 4. Expected values for actual observations are presented in section 5, and final section is devoted to discussions.

---

[1] Surface mass density on images of gravitationally lensed quasars is estimated to be order of critical surface mass density of the lens systems. Additionally, the surface mass density is not so much different in different system. Therefore, optical depth for quasar microlensing should be order of unity, if most of the mass consists from stellar objects.

2. Suitable Lens System to Detect CDM Substructures

In previous works, the detectability of substructure around galaxies are only considered in the case of gravitationally lensed quasars. Here, we go back to the first step and briefly discuss about the most suitable system to probe substructure around galaxies. Luminosity or surface brightness of substructures should be quite faint and unknown, and we investigate the method to probe substructures as not the source but the lens. In the following argument, we fix total number of substructures (N_{sub}), mass of individual substructures (M_{sub}), and the size of host galaxies of substructures (R_{host}) in all galaxies, for simplicity. If we take into account more realistic situations, the following argument for our current purpose will not dramatically change.

The most essential quantity to estimate the detectability of gravitational lens effect is the optical depth for gravitational lensing, Υ. This value is identical to the surface mass density of lens objects in the unit of critical surface mass density or the coverage fraction by the typical size of gravitational lens on the sky. If we put the host galaxy at the angular diameter distance D_{ol}, substructures will exist roughly in the region with $S_{host} \sim \pi(R_{host}/D_{ol})^2$ radian^2. On the other hand, we consider the lens objects as the point mass and the typical lens size is evaluated by Einstein ring radius (θ_E) which is expressed as

$$\theta_E = \left(\frac{4GM_{sub}}{c^2}\frac{D_{ls}}{D_{ol}D_{os}}\right)^{1/2}, \tag{1}$$

where D_{ls} and D_{os} is the angular diameter distance between the lens and the source and the observer to the source, respectively. By using this typical lens size, the total coverage by substructure lenses on the sky is $S_{lens} \simeq N_{sub} \cdot \pi\theta_E^2 = 4\pi N_{sub}GM_{sub}D_{ls}/(c^2 D_{ol}D_{os})$ radian^2. Consequently, the optical depth (Υ) is evaluated as follows,

$$\Upsilon = \frac{S_{lens}}{S_{host}} \sim N_{sub}\frac{4GM_{sub}}{c^2 R_{host}^2}\frac{D_{ls}D_{ol}}{D_{os}}. \tag{2}$$

The equation means that the distant lens system has larger optical depth for gravitational lensing except some special case such as self-lensing, i.e., $D_{ol} \sim D_{os}$. For example, the Gpc-scale lens systems have three orders of magnitude larger optical depth than the Mpc-scale lens systems. Therefore, distant galaxies are more preferable to our purpose rather than the Milky Way galaxy, and gravitationally lensed quasars seem to be better candidate to probe substructures around galaxies.

Additionally, to utilize gravitational lensing, substructures as lens objects should be close to the line of sight to the sources. substructures are not distributed uniformly in universe but clustered around their host galaxy, and the line of sight to the source should intersect in the vicinity of galaxies. e.g., light from the source passes inside R_{host} from the center of the host galaxy. In this point of view, we can also say that gravitationally lensed quasars are the most suitable system to probe substructures, because such systems automatically satisfy this

condition. We will present more detailed discussion about optical depth for strong lensing by CDM substructures in section 5.2.

3.   Calculation Methods

Expected phenomena for gravitational lensing depend on the situation, lens model, some observational constraints and so on. To evaluate expected values for image separation and time delay between further multiple images, we describe adopted calculation methods for our estimations in this section. Recently reported cosmological parameters measured by WMAP (Spergel et al. 2003) is adopted here, i.e., $\Omega_m = 0.3$, $\Omega_\Lambda = 0.7$, and $H_0 = 70$ km s^{-1} Mpc^{-1}. We set $z_l = 1$ (the lens redshift), $z_s = 2$ (the source redshift), $M_{sub} = 10^7 M_\odot$ (or a corresponding velocity dispersion [2]) for a representative case unless otherwise specified.

3.1.   Assumptions and constraints for estimations

In the strong lensing regime for a single lens object, i.e., a substructure, the external effects may dramatically change the properties of the lens object as a gravitational lens. The most important effects are external convergence and shear. Generally, such external effects are caused by additional objects around the main lens object, a substructure in this case. There are two possible source to produce such effects in current situation. One is the host galaxy of substructures. As is well known in the argument for quasar microlensing and/or for constructing the macrolens model for gravitationally lensed quasars, the convergence around an image of gravitationally lensed quasars estimated to be order of unity (e.g., see Schmidt, Webster & Lewis 1998). Moreover, the shear is roughly the same value as the convergence. In such situations, even if the object is compact enough we can no more treat the main object as simple point mass lens, and we have to treat the lens as so-called "Chang - Refsdal" lens developed by Chang & Refsdal (1984). Particularly, the shear effect dramatically change the lens properties and magnification pattern becomes cuspy asteroid shape from circular shape, though the convergence effect is the simple focusing of the lens and the source planes. Thus, we include external convergence and shear effect in our calculation. Since the typical lens size of substructures is much smaller than that of the host galaxy, we assume the external convergence and shear are constant. The magnification patterns in the case of "Chang - Refsdal" lens model are shown in figure 1. Details for lens models are shown in section 3.2.

Another possible source to produce external effects is other structures, i.e., other substructures in the vicinity of the main substructure. If the lens plane is crowded with substructures and the optical depth is almost equal to or larger than unity, the gravitational lens properties such as magnification pattern will become very complicated similar to quasar microlensing (e.g., Wambsganss, Paczyński, & Schneider 1990). By using equation 2, results

---

[2]   From the spherical collapse model that the collapse redshift is ~ 20, the velocity dispersion (σ) for such object is expressed as $v_{sub} \sim 11.0(M/10^7 M_\odot)^{1/3}$ km s^{-1} (Padmanabhan 1993).
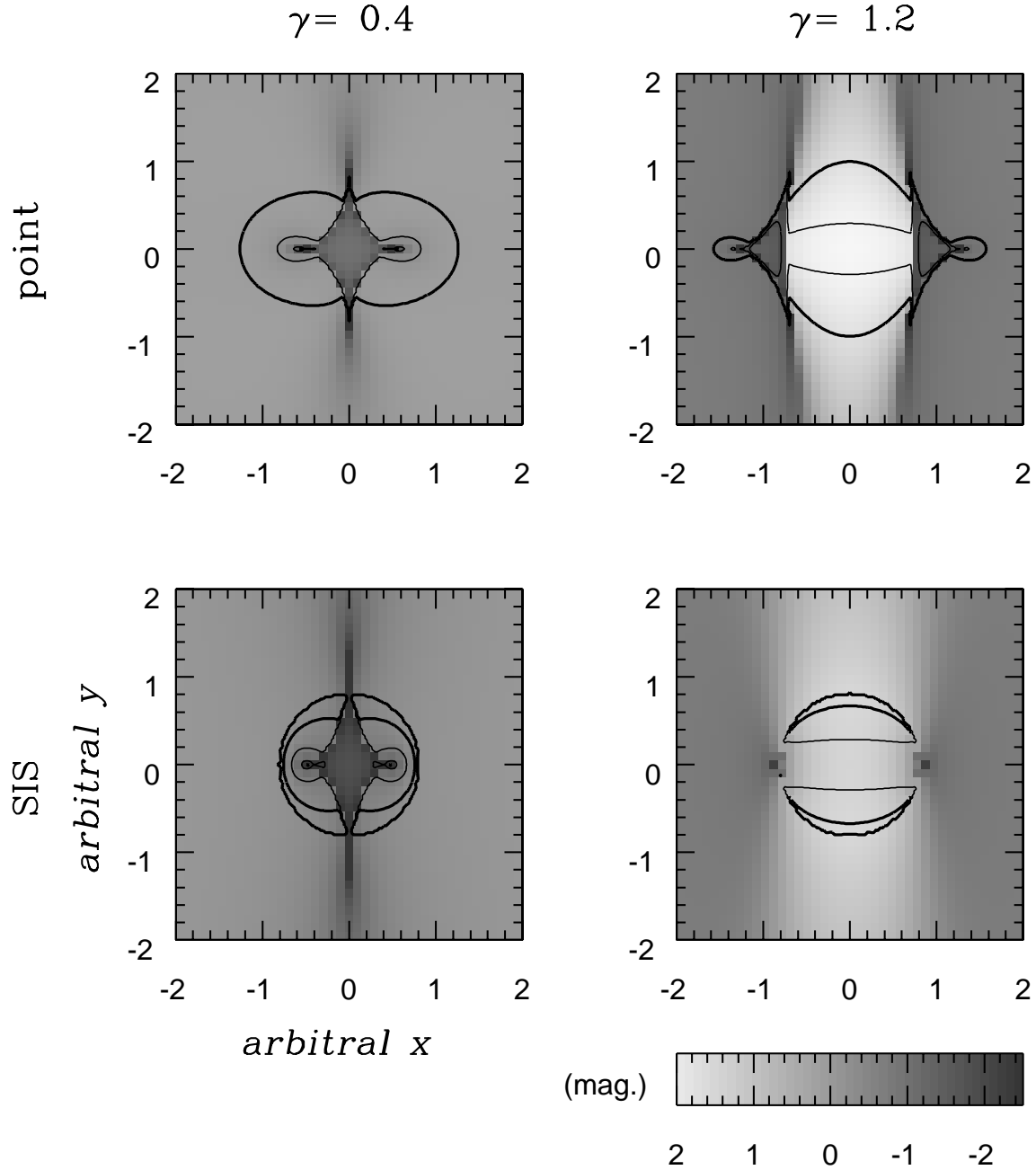
Fig. 1. Magnification patterns of "Chang & Refsdal" lens for point mass lens (upper two panels) and for singular isothermal sphere (SIS) lens (lower two panels) are presented. The gray scale is in the unit of magnitude as shown at the bottom. Here, the external convergence (κ) is equal to zero and the external shear (γ) is 0.4 in the left panels and 1.2 in the right panels [3]. The unit of $x-$ and $y-$axis is the typical lens size, e.g., Einstein ring radius for point mass lenses. Thin and thick lines show the contour for $f_{\mathrm{lim}} = 2.0$ and $= 10.0$, respectively, where f_{lim} is the flux ratio between the brightest two images (see text).

obtained by numerical simulations (e.g., $N_{\rm sub} \sim 10^3$ inside $R_{\rm host} \sim 140$ kpc), and put an arbitral mass for substructure, we are able to check the expected optical depth for substructure lens. There are some uncertainty due to lens properties, but if we set $M_{\rm sub} \sim 10^7 M_\odot$, the expected value will become $\sim 10^{-4}$. As investigated by previous estimation (e.g., Lee & Spergel 1990), probability distribution for shear (γ) which produced by ensemble of point mass lenses with an average dimensionless surface mass density (κ_*), $\tilde{p}(\gamma, \kappa_*)$, is expressed as

$$\tilde{p}(\gamma, \kappa_*) = \frac{\kappa_* \gamma}{\left(\kappa_*^2 + \gamma^2\right)^{3/2}}. \tag{3}$$

Thus, cumulative probability distribution to produce a shear less than γ, $p(<\gamma|\kappa_*)$, is evaluated as follows,

$$p(<\gamma|\kappa_*) = \int_0^\gamma \tilde{p}(\gamma', \kappa_*) d\gamma' = 1 - \frac{\kappa_*}{\left(\kappa_*^2 + \gamma^2\right)^{1/2}}. \tag{4}$$

κ_* is equivalent with Υ in current situation, and $p(<\gamma|\kappa_*) \sim 0.9$ for $\gamma \sim 10\Upsilon$. In other words, effect of other substructures close to the main substructure is mostly less than 10^{-3} as an additional external shear. Even if we set $M_{\rm sub} \sim 10^9 M_\odot$, the expected external shear will be 0.1. These values are small compared with external shear produced by the host galaxy of substructures, and we may safely be able to treat a substructure as an isolated lens object. More detailed arguments are presented in section 5.2, and will validate this "single isolated lens" treatment or "Chang - Refsdal" lens treatment.

As we have already noted in section 1, the target systems in our estimations, i.e., gravitationally lensed quasars, frequently suffer quasar microlensing and flux of images can be fluctuate around some median value with fairly long time scale. However, we are mainly focus not on magnification but on image separation and time delay between further multiple images. Since these two quantities are directly reflect the typical lens size and the size of stellar mass objects is several orders of magnitude smaller than that of substructures, the perturbation caused by stellar mass objects for quasar microlensing is negligibly small. Then, we do not include any effect due to quasar microlensing.

Finally, we have to mention about flux ratio between the primary brightest image (A_1) and the secondary brightest image (A_2), $f_{\rm lim} = A_1/A_2$, that is an important constraint to our estimations and will closely relate to the actual observational difficulties. To detect substructures by utilizing strong gravitational lensing, we have to hunt signals from further multiple images created by strong gravitational lens effect by CDM substructures. As schematically presented in figure 2, we will find further multiple images beside one of multiple images of gravitationally lensed quasars with fine spatial resolution. Even if we cannot resolve further multiple images, we may be able to observe flux variation of a further multiple image superposed on that of another image. Such phenomenon will be observed as "echo"-like flux variations in intrinsic variabilities of quasars. Since time lags of the "echo"-like flux variation should be correspond to time delay between further multiple images, the measurement of the "echo" time lag is iden-

7

images of
gravitationally
lensed quasars

CDM substructure
exist in the vicinity
of one of the images

CDM
substructure

Further multiple images
are newly created

Even if images are
not spatially resolved

Intrinsic flux variation

Observed flux variation

"Echo"-like variation
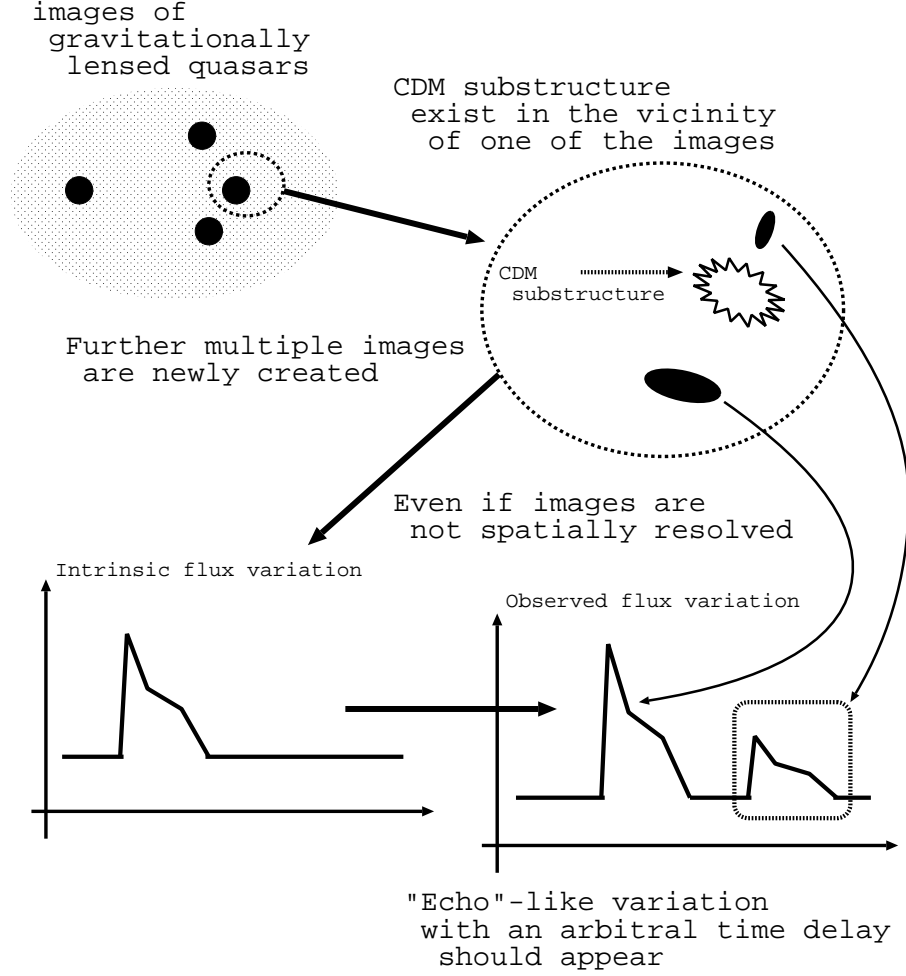with an arbitral time delay
should appear

Fig. 2. Schematic picture of phenomena expected in strong lensing effects by substructures.

tical to the measurement of time delay between further multiple images. Such measurement can be direct evidence for substructures around galaxies. However, actual observations suffer many kind of noises caused by detector, background objects, air glow and so on. Therefore, if the secondary brightest image is too faint compared with the primary brightest image, the "echo"-like signal from the secondary brightest image may be smeared out in noises and we will not be able to find any evidence for substructure. To take into account such observational difficulties, we put some limits on f_{lim}. Contours for some constant f_{lim} are presented in figure 1 for some cases.

3.2. Lens models

For "Chang - Refsdal" lens treatment, the lens equation with external convergence (κ) and shear (γ) is written as

$$\vec{\beta} = (1-\kappa)\vec{\theta} - \gamma(\theta_x, -\theta_y) - \vec{\alpha}(\vec{\theta}), \tag{5}$$

where $\vec{\theta} = (\theta_x, \theta_y)$ and $\vec{\alpha}$ are arbitrary locations on the lens plane and bending angle at the

location, respectively. The shear direction in this formula is parallel to x-axis. Solving this equation for a given $\vec{\beta}$, we obtain all the location of multiple images and can calculate separations between images. For image 1 at location $\vec{\theta_1}$ and image 2 at location $\vec{\theta_2}$, the image separation ($\Delta\theta_{1,2}$) is calculated from $\Delta\theta_{1,2} = \left|\vec{\theta_1} - \vec{\theta_2}\right|$. By using lens potential (Ψ), arrival time delay (Δt) from the light path without gravitational lens effect is written as

$$\Delta t = \frac{1+z_l}{2}\frac{1}{c}\frac{D_{ol}D_{os}}{D_{ls}}\left[\left(\vec{\theta} - \vec{\beta}\right)^2 - \kappa\left|\vec{\theta}\right|^2 - \gamma\left(\theta_x^2 - \theta_y^2\right) - 2\Psi(\vec{\theta})\right]. \tag{6}$$

Time delay between images is the arrival time delay difference between images, and we obtain time delay by subtracting Δt at an image from Δt at other images. Thus, for image 1 at location $\vec{\theta_1}$ and image 2 at location $\vec{\theta_2}$, the time delay ($\tau_{1,2}$) is calculated from $\tau_{1,2} = \Delta t(\vec{\theta_1}) - \Delta t(\vec{\theta_2})$. Here, we apply two kind of lens models for substructures, one is point mass lens model and another is singular isothermal sphere (SIS) lens model (see section 6.1 for discussion about lens model).

For point mass lens model, the typical lens size is given by Einstein ring radius, θ_E (see equation 1), and the bending angle ($\vec{\alpha}$) at an arbitrary location on the lens plane ($\vec{\theta}$) is expressed as

$$\vec{\alpha} = \left(\frac{\theta_E}{\left|\vec{\theta}\right|}\right)^2\vec{\theta}. \tag{7}$$

Additionally, the lens potential is given as follows

$$\Psi = \theta_E^2\ln\left|\vec{\theta}\right|. \tag{8}$$

For substructures with $M_{sub} = 10^7 M_\odot$, θ_E and $\theta_E^2\frac{1+z_l}{2}\frac{1}{c}\frac{D_{ol}D_{os}}{D_{ls}}$ are equal to 4.23 mas and 1.97×10^2 s, respectively.

In contrast, for SIS lens model, the typical lens size, θ_{SIS}, is given as following form,

$$\theta_{SIS} = 4\pi\left(\frac{v_{sub}}{c}\right)^2\frac{D_{ls}}{D_{os}}, \tag{9}$$

where v_{sub} is the velocity dispersion of substructures. The bending angle and the lens potential in this case is presented as

$$\vec{\alpha} = \frac{\theta_{SIS}}{\left|\vec{\theta}\right|}\vec{\theta} \tag{10}$$

and

$$\Psi = \theta_{SIS}\left|\vec{\theta}\right|, \tag{11}$$

respectively. For substructure with $\sigma_{sub} = 11.0$ km s^{-1}, θ_{SIS} and $\theta_{SIS}^2\frac{1+z_l}{2}\frac{1}{c}\frac{D_{ol}D_{os}}{D_{ls}}$ are equal to 1.27 mas and 1.78×10^1 s, respectively.

To evaluate actual values for given redshifts and mass or velocity dispersions, it is not efficient to perform calculations for all parameter combinations. As shown in appendix 1, image
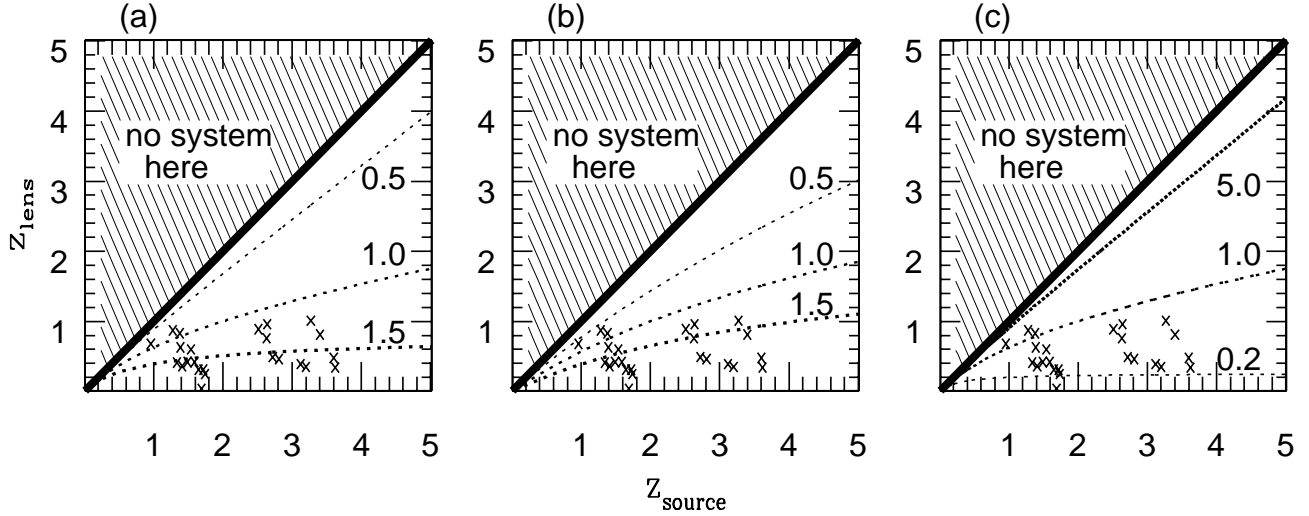
9

Fig. 3. The lens and the source redshifts dependences of typical lens size for point mass lens, $\theta_{\rm E}$ (left panel, a), for SIS lens (middle panel, b), and for the time delay (right panel, c) are presented. Dotted lines in left panel (a) and middle panel (b) show contours for $\theta_{\rm E}(z_{\rm l}, z_{\rm s})/\theta_{\rm E}(z_{\rm l}=1, z_{\rm s}=2)$ or $\theta_{\rm SIS}(z_{\rm l}, z_{\rm s})/\theta_{\rm SIS}(z_{\rm l}=1, z_{\rm s}=2)$ $= 0.5$ (thin line), 1.0 (middle line), and 1.5 (thick line). Dotted lines in right panel (c) show contours for $(1 + z_{\rm l})D_{\rm ol}D_{\rm os}/D_{\rm ls} = 0.2$ (thin line), 1.0 (middle line), and 5.0 (thin line) times larger than that for $(z_{\rm l}, z_{\rm s}) = (1, 2)$ for right panel (c). Cross symbols show currently known, redshifts measured lens systems. Since redshift of the lens should be smaller than that of the source, there is no lens system at the upper-left shaded region, $z_{\rm l} \geq z_{\rm s}$.

separation and time delay have scaling laws for typical lens sizes, and it must be convenient to utilize such scaling laws.

Image separations are simply proportional to $\theta_{\rm E}$ for point mass lens and to $\theta_{\rm SIS}$ for SIS lens. For point mass lens, it is apparent that $\theta_{\rm E}$ is proportional to mass of substructures. System-to-system variance or redshifts dependence of $\theta_{\rm E}$ is shown in figure 3 (a). At least for currently known lens systems, $\theta_{\rm E}$ values are factor of ~ 2 variance and system-to-system variance of expected image separations is not negligible but small. For SIS lens, $\theta_{\rm SIS}$ is proportional to square of velocity dispersion of substructures. System-to-system variance of $\theta_{\rm SIS}$ is also shown in figure 3 (b). Again, system-to-system variance is not negligible but small.

Time delays are proportional to square of $\theta_{\rm E}$ for point mass lens, and to square of $\theta_{\rm SIS}$ for SIS lens. Thus, dependence of $\theta_{\rm E}$ and $\theta_{\rm SIS}$ is $M_{\rm sub}^2$ for point mass lens and $\sigma_{\rm sub}^4$ for SIS lens, respectively. However, system-to-system variance is not so simple as the image separations, because we should take into account another term including system redshifts (e.g., see equation 6). The effect of this additional term is presented in figure 3 (c). Gradient of this contour is roughly inverse of that in figure 3 (a) and 3 (b), and this additional effect will partly cancel out. Particularly, for point mass lens, angular diameter distances are completely cancel out and only $(1 + z_{\rm l})$ term remains as system-to-system variance.

Consequently, system-to-system variance is not so large, and our estimations present

below will straightforwardly be applicable to any lens systems. If you require more detailed values, you will refer figure 3, and will simply multiply proper factors to our results.

3.3. Numerical methods

To estimate probability distributions for image separation and time delay between two brightest images, we performed Monte-Carlo simulation as follows;

1. The source position is randomly determined within a circle. The maximum radius for the source position is determined that all region satisfies a required condition such as constraint on $f_{\rm lim}$ is included.
2. Solving the lens equation, we obtain all image positions and corresponding magnification factors for the given source position. Selecting the brightest two images, we calculate flux (f) ratio between the brightest two images.
3. If the flux ratio is smaller than a given constraint, i.e., $f \leq f_{\rm lim}$, the fainter image can also be observable and we will continue further calculation for obtaining probability distributions. Therefore, resultant probabilities are conditional probabilities. If the flux ratio is larger than a given constraint, we will go back to the first step and perform the same calculation again for other source position.
4. By using the source position which satisfy our constraint, we can easily evaluate image separation, $\Delta\theta_{1,2}$, and time delay, $\tau_{1,2}$, from equation 5 and 6, respectively.

Repeat the above procedures (step $1 \sim 4$) for many times, and we obtain probability distributions for image separation and time delay. In this paper, we perform 50000 realizations. To achieve good accuracy for our calculations, the maximum radius for the source is large enough. On the other hand, to perform efficient calculations, the radius should not be too large. Then, we determine the maximum radius for the source positions by referring magnification patterns and contours of flux ratio such as presented in figure 1. Though calculations for image separation and time delay are straight forward after we obtain image positions, calculations for image positions at a given source position are not, caused by the nature of lens equation. To overcome this difficulty, we adopt a proper method which utilizing so-called "ray-shooting" (e.g., Keeton 2001). Our numerical code solve the lens equation with sufficiently good accuracy.

4. Individual Lens Properties

Here, we present probability distributions for image separation and time delay for different γ, κ, and $f_{\rm lim}$ in the case of a single substructure, i.e., only one value for $\theta_{\rm E}$ and $\theta_{\rm SIS}$. Hereafter, cumulative distribution for quantity x is presented as $p(<x|\kappa,\gamma)$. The reasons for dependences on the parameters are also discussed in this section. To make situation clear, we consider a few representative value for each parameter. Detailed values of our estimations or
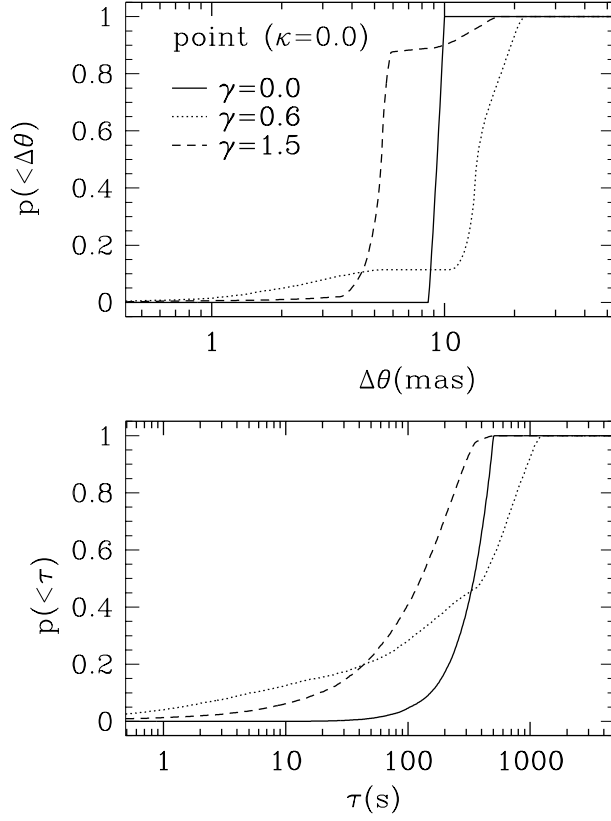
Fig. 4. Cumulative probability distribution of image separation (upper panel) and that of time delay (lower panel) are presented in the case of point mass lens model. Solid, dotted, and dashed lines indicate $\gamma = 0.0$, 0.6, and 1.5, respectively. Unit of the abscissa is milliarcsecond for image separation and second for time delay. The scales of the abscissa are logarithmic.

estimated values for other parameter sets are obtained via WWW. [4]

4.1. Effect of shear

First of all, we fix external convergence value as $\kappa = 0$ and calculate probability distributions to investigate the effects of external shear for point mass lens case. Cumulative probability distribution of image separation ($\Delta\theta$) and time delay (τ) are presented in figure 4. As is clear from figure 1, the lens properties dramatically change from $\gamma < 1$ case to $\gamma > 1$ case, and we present the result of $\gamma = 0.6$ as a representative case for $\gamma < 1$ and that of $\gamma = 1.5$ as a representative case for $\gamma > 1$.

Compared with no-shear case ($\gamma = 0$), the shape of distribution dramatically changed and the range of distribution is extended toward large and small $\Delta\theta$ as depicted in upper panel of figure 4. Though the lowest value of the distribution become small, the most part of the distribution shifted toward large $\Delta\theta$ direction by some factor. The shear effect will make the detection of quasar mesolensing signal easier. However, if the shear is too large and exceed

---

[4] ULR is http://www.rccp.tsukuba.ac.jp/Astro/yonehara/research.subhalo.html

12

unity, e.g., $\gamma = 1.5$, the most part of the distribution shifted toward small $\Delta\theta$ direction by some factor. Therefore, too large shear will make the detection of quasar mesolensing signal more difficult.

Since time delay is directly affected by image separation (see equation 6), the dependence on the external shear is similar to the image separation as depicted in lower panel of figure 4. The shape of the distribution of time delay is apparently different from that of the image separation, but qualitative features are the same. In large γ case, the distribution extends toward large and small τ direction, and larger time delay will be expected compared with no-shear case. On the other hand, the distribution shifted toward small τ direction in the case of γ exceed unity again and the substructure detection via quasar mesolensing will become difficult.

4.2. Model dependence

Here, we present the expected values for SIS lens model. Before discussing the probability distribution, we briefly mention about basic properties of SIS lens model. It is well known that SIS lens produces pseudo-caustics [5] at $|\vec{\beta}| = \theta_{\mathrm{SIS}}$. Generally, image separation increases with the source separate from the lens (detailed explanations are presented in section 4.4). If the source locate outside both of caustics and pseudo-caustics, only one image appears, and we cannot define any quantities relate to our current estimations. Thus, different from the point mass lens, image pair cannot separate so large in the case of SIS, and the distribution shows sharp drop/rise at large value compared with point mass lens case, as presented in figure 5.

It is apparent that the resultant cumulative distributions show different shape from that for point mass lens case. This is partly due to the unique nature of SIS lens model that we mentioned just before. Additionally, expected values are smaller than that for point mass lens case by a several factor. However, the dependence on external shear is qualitatively same as that for point mass lens case, i.e., large external shear makes expected values large but too large external shear, $\gamma \geq 1$, makes expected values small. There is no essential difference between these two lens models, and we mainly focus on point mass lens model at the following part.

4.3. Effect of convergence

As is already noted by Falco, Gorenstein & Shapiro (1985), external convergence leads degeneracy problem for modeling of lens objects. In contrast, if we fix lens model as current estimations, thanks to the simple nature of convergence, effects of external convergence can be easily take into account as proper scaling laws.

Clearly, the convergence term in equation 5 will eliminate, if we divide both side of the equation by $(1 - \kappa)$. After eliminating the convergence term, the lens equation becomes similar form again, and the shear term changes from γ to $\gamma_{\mathrm{eff}} = \gamma/(1 - \kappa)$. Following some algebra as

---

[5]   If the source crosses pseudo-caustic (sometime it is called "cut"), only one image will appear/disappear. In contrast, if the source crosses usual caustic, two image with same flux but different parity will appear/disappear as a pair.
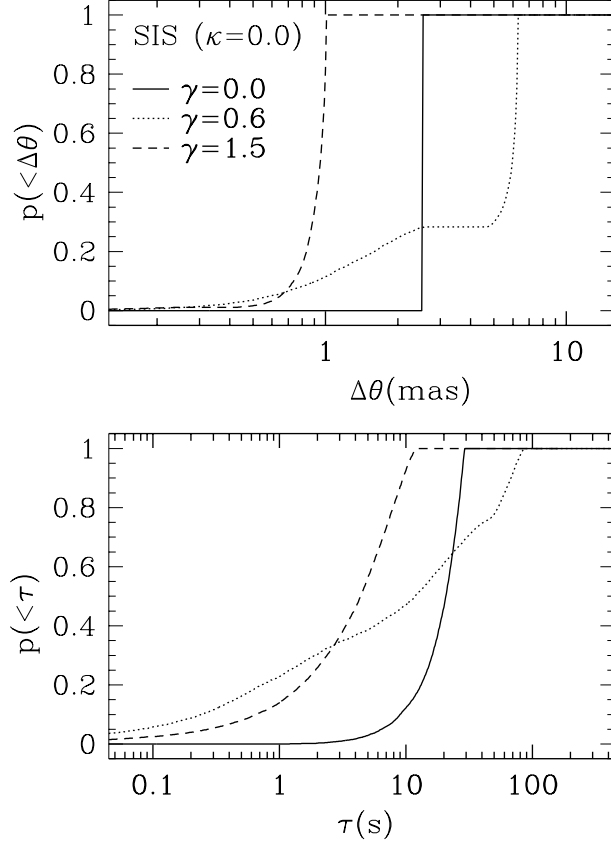
Fig. 5. Same as figure 4, but for SIS lens model.

presented in appendix 2, we obtain the scaling laws of $\Delta\theta$, τ, and μ_{tot} (total magnification) [6] for point mass lens model as

$$p(<\Delta\theta|\kappa,\gamma) = p\left(<\frac{\Delta\theta}{(1-\kappa)^{0.5}}\bigg|0,\gamma_{\text{eff}}\right), \tag{12}$$

$$p(<\tau|\kappa,\gamma) = p(<\tau|0,\gamma_{\text{eff}}), \tag{13}$$

$$p(<\mu_{\text{tot}}|\kappa,\gamma) = p\left(<\frac{\mu_{\text{tot}}}{(1-\kappa)^2}\bigg|0,\gamma_{\text{eff}}\right), \tag{14}$$

and that for SIS lens model as

$$p(<\Delta\theta|\kappa,\gamma) = p\left(<\frac{\Delta\theta}{(1-\kappa)}\bigg|0,\gamma_{\text{eff}}\right), \tag{15}$$

$$p(<\tau|\kappa,\gamma) = p\left(<\frac{\tau}{(1-\kappa)}\bigg|0,\gamma_{\text{eff}}\right), \tag{16}$$

$$p(<\mu_{\text{tot}}|\kappa,\gamma) = p\left(<\frac{\mu_{\text{tot}}}{(1-\kappa)^2}\bigg|0,\gamma_{\text{eff}}\right). \tag{17}$$

Therefore, to obtain the distributions for non-zero convergence and shear, γ, case, we calculate zero convergence with equivalent effective shear, $\gamma_{\text{eff}} = \gamma/(1-\kappa)$, case, and horizontally shift
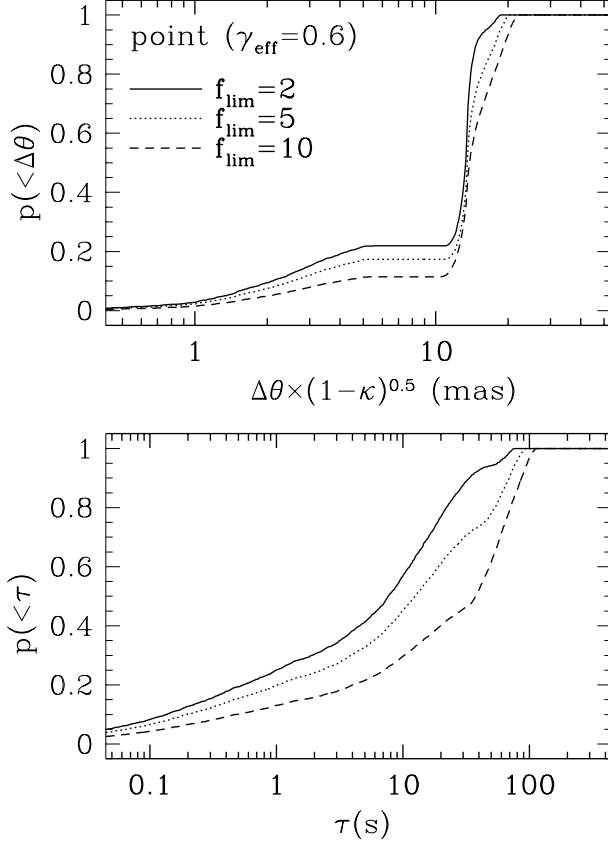
---

[6]   Absolute values for all image are summed up.

14

Fig. 6. Same as figure 4, but for different f_{lim} case. Solid, dotted, and dashed lines show $f_{\text{lim}} = 2$, 5, and 10 case, respectively. The effective shear is fixed at $\gamma_{\text{eff}} = 0.6$.

the resultant distributions by a proper factor.

4.4. Flux ratio difference

At the end of this section, we present dependence on our assumed value for f_{lim} that will mimic constraint for real observations. Here, we already have scaling laws for convergence, fixed shear value as $\gamma_{\text{eff}} = 0.6$ and present the resultant distributions for $f_{\text{lim}} = 2$, 5, and 10 case in figure 6.

In upper panel of figure 6, image separation, the shape of the distribution does not change so much in horizontal direction but changes toward downward slightly with increasing f_{lim}. Then, the expected values becomes large with increasing f_{lim}. The reason is easily understood from the following analogy. The source separate enough from the lens, number of images becomes two. The more the source and the lens separates, the more these two images separates because one image is formed near the original source position, or the source position without lens effect, and another image is formed near the lens position. At the same time, since the image near the original source position becomes faint toward the original source flux, i.e., lower limit is the original source flux, since another image near the lens position becomes faint

toward infinitely small flux, i.e., lower limit is zero. The image near the original source is usually brighter than another image, and finally, f_{lim} increase toward infinity with the source and the lens separation. If we allow large value for f_{lim}, it will be comparable to the situation that we can observe fainter images. In such a case, we can observe more separate image pairs as the above argument, and the expected image separation becomes large. However, the fainter image becomes rapidly faint with the source and the lens separation, and change of the distribution is not significantly.

Due to the same reason, the distribution of time delay only slightly changes with f_{lim} as clearly shown in lower panel of figure 6. Time delay relates to $\Delta\theta^2$ rather than $\Delta\theta$, and difference between the distribution for different f_{lim} seems to be large compared with that of image separation. We note that the expected value becomes large with increasing f_{lim}, again.

5. Actual Lens Properties of CDM Substructures

Employing basic properties for quasar mesolensing that presented in the previous section, we can evaluate really expected value for image separation and time delay due to quasar mesolensing including statistical properties of substructures.

5.1. Expected values

To obtain expected values in a real situation, we have to include mass or velocity distribution of substructure. As shown previous sections, probability distributions are determined by M_{sub} (or v_{sub} for SIS lens) via the lens size, κ, γ, and f_{lim}. If we put mass and velocity distribution [7] for number of substructures as $n(M)$ and $n(v)$, respectively, really expected, cumulative distributions for point mass lens case $p_{\text{E}}(<x)$ and for SIS lens case $p_{\text{SIS}}(<x)$ will be written as

$$p_{\text{E}}(<x) = \frac{\int_{M_{\text{l}}}^{M_{\text{u}}} p_{\text{E}}(M|<x)n(M)dM}{\int_{M_{\text{l}}}^{M_{\text{u}}} n(M)dM}, \tag{18}$$

and

$$p_{\text{SIS}}(<x) = \frac{\int_{v_{\text{l}}}^{v_{\text{u}}} p_{\text{SIS}}(v|<x)n(v)dv}{\int_{v_{\text{l}}}^{v_{\text{u}}} n(v)dv} \tag{19}$$

where, $p_{\text{E}}(M|<x)$ and $p_{\text{SIS}}(v|<x)$ are cumulative distributions for a given mass or velocity of substructures in the case of point mass lens and SIS lens, respectively. M_{l}, M_{u}, v_{l}, and v_{u} are lower limit and upper limit for mass of substructures and that for velocity of substructures, respectively.

Here, we assume power-law for $n(M)$ and $n(v)$, i.e., $n(M) \propto M^a$ and $n(v) \propto v^b$. Adopting the resultant power-law index obtained by cosmological N-body simulations (Klypin et al. 1999), we set $a = -1.92$ and $b = -3.75$. Upper limits for substructures are sufficiently above the

---

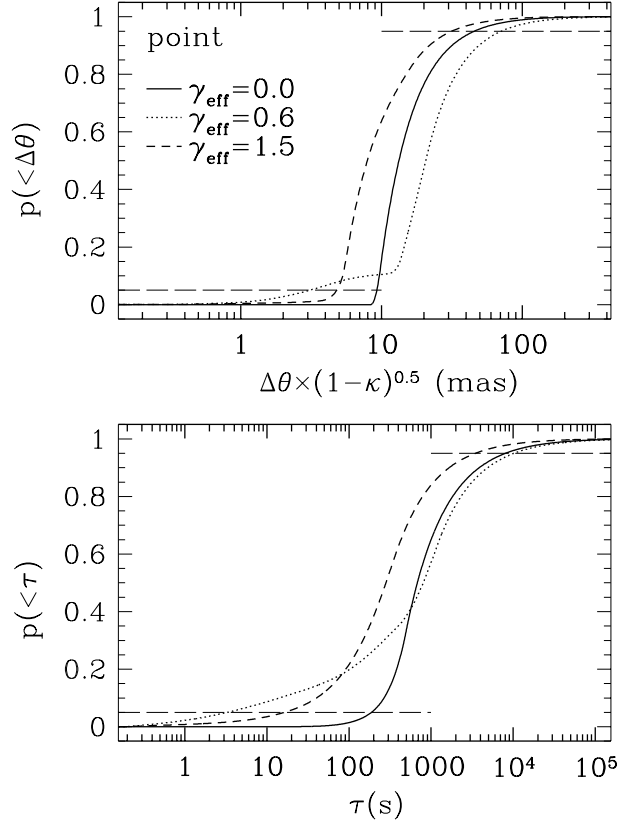[7]   These are so-called "mass function" and "velocity function", and not cumulative ones.

Fig. 7. Same as figure 4, but for mass distribution for substructures is taken into account. Thin long-dashed lines show $p(< \Delta\theta) = 0.05$ (lower line) and 0.95 (upper line). This is point mass lens case.

resolution of the simulation. In contrast, lower limits are comparable to the current resolution (around $10^7 M_\odot$ or 11 km s^{-1}) and somewhat unclear. Of course, if we include small mass (or velocity) scale, number of substructures will increase and optical depth for quasar mesolensing will also increase. However, the expected image separation and time delay for such small scale structure should be small, and it can be difficult to detect. Therefore, we only take into account the mass and the velocity range for the previous simulations, and set $M_l = 10^7 M_\odot$, $M_u = 10^{10} M_\odot$. For the velocity range, we apply that the range corresponds to that of the mass range, and set $v_l = 11$ km s^{-1} and $v_u = 110$ km s^{-1}. The resultant distributions are presented in figure 7 for point mass lens case and in figure 8 for SIS lens case. The distributions for various γ_{eff} are presented in these figures. In abscissa, we include κ dependence discussed in section 4.3 for convenience. For example, if we want to know the distribution of the image separation for $\kappa = 0.5$ in the case of SIS lens model, 1 mas and 1 s in figure 8 will correspond to 1 mas$/(1-0.5) = 2$ mas and 1 s$/(1-0.5) = 2$ s, respectively.

Comparing upper panels of figure 7 and 8, the expected image separations for point mass lens are slightly larger than that for SIS, but seems to be ~ 1 mas for lower limit and ~ 30 mas for upper limit. These values are comparable or smaller than spatial resolution of current observational instruments, but some future observational facilities will achieve this resolution
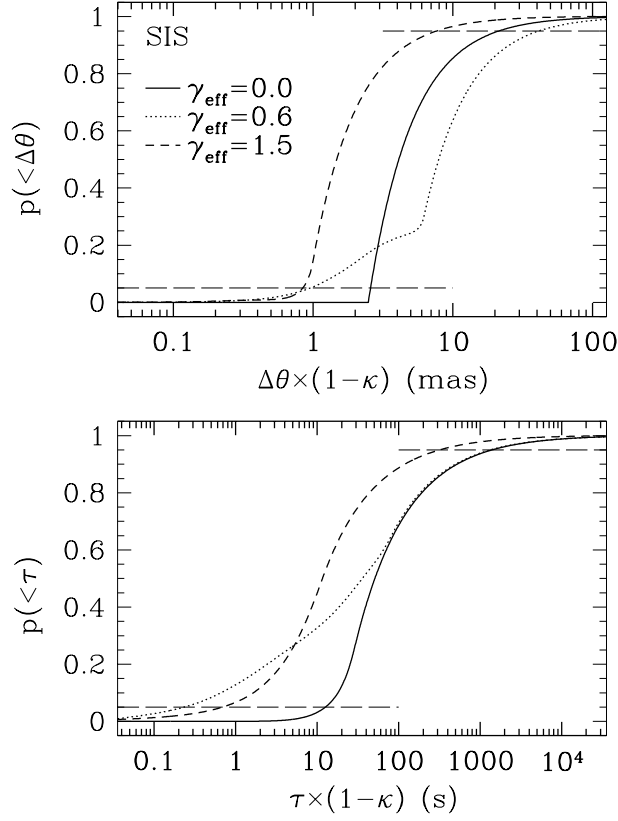
17

Fig. 8. Same as figure 5, but for velocity distribution for substructures is take into account. Thin long-dashed lines show $p(< \tau) = 0.05$ (lower line) and 0.95 (upper line). This is SIS lens case.

(see also discussion).

The expected time delays are also shown in lower panels of figure 7 and 8. Reflecting the difference of image separation, the expected time delay for point mass lens is larger than that of SIS lens, again. Difference between different lens model and different $\gamma_{\rm eff}$ is somewhat larger, but lower value for time delay is ~ 1 s and upper value is $\sim 10^3$ s. Of course, even in the case of $\sim 10^3$ s, it is not easy task to find echo-like flux variation due to quasar mesolensing in quasar variabilities with stochastic feature. However, this sub-day level time delay may be found by some coordinated monitoring observations in future (see also discussion).

5.2. Probabilities for the strong lensing

Reality for quasar mesolensing is evaluated by optical depth of gravitational lensing due to substructure. It can be roughly estimated from equation 2. More exact optical depth are written as

$$\Upsilon = \frac{1}{S_{\rm host}} \frac{1}{(1-\kappa)^2 - \gamma^2} \int_{M_{\rm l}}^{M_{\rm u}} \sigma_{\rm lens}(M) n(M) dM, \tag{20}$$
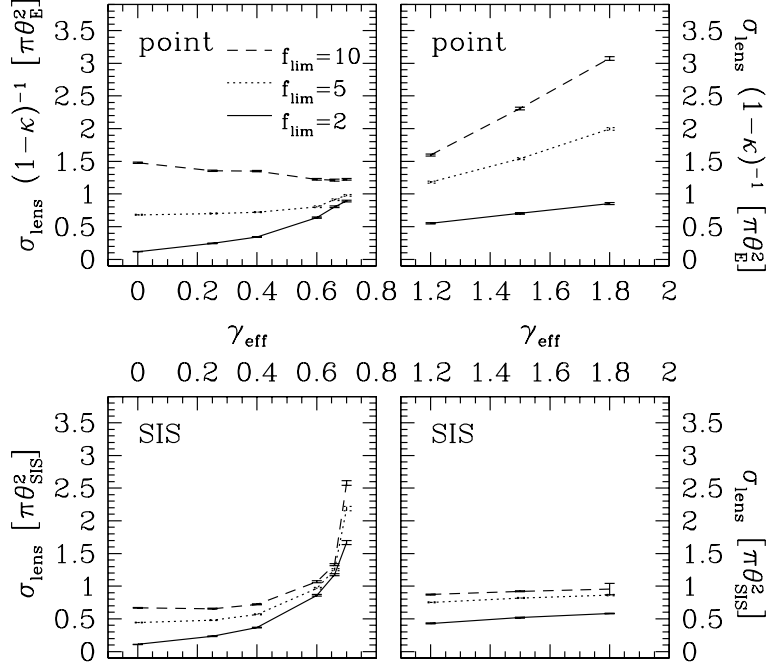
for point mass lens, and

Fig. 9. Cross sections of quasar mesolensing for various $\gamma_{\rm eff}$ are presented in this figure. Unit for the cross section is $\pi\theta_{\rm E}^2$ for point mass lens and $\pi\theta_{\rm SIS}^2$ for SIS lens. Upper two panels show point mass lens case, and lower two panels show SIS lens case. Left panels are the case for $\gamma < 1$, though right panels are the case for $\gamma > 1$. Solid, dotted, and dashed lines show the cross section for $f_{\rm lim} = 2$, 5, and 10, respectively.

$$\Upsilon = \frac{1}{S_{\rm host}} \frac{1}{(1-\kappa)^2 - \gamma^2} \int_{v_{\rm l}}^{v_{\rm u}} \sigma_{\rm lens}(v) n(v) dv, \tag{21}$$

where $\sigma_{\rm lens}$ denotes cross section of quasar mesolensing for a given lens mass or lens velocity. The second fraction term in the right-hand side is the stretching effect of source plane and similar to so-called "magnification bias". Column number density of substructures is estimated in the lens plane, but the lens plane have already been magnified by a factor identical to this term, $\{(1-\kappa)^2 - \gamma^2\}^{-1}$ [8]. If we trace back to a region from the lens plane to the source plane, the surface area will become small by this factor. Consequently, column number density of substructures is increased by a factor $\{(1-\kappa)^2 - \gamma^2\}^{-1}$. Cross section of quasar mesolensing for a given mass or velocity strongly depends on κ, γ, and other constraints ($f_{\rm lim}$ in this case). Thus, it is difficult to calculate the cross section analytically in current situation (but see Keeton 2003 for similar situations), and we evaluated it by using our Monte-Carlo simulation. The results are shown in figure 9.

For κ dependence, we can derive from scaling law for $\vec{\beta}$ between non-zero convergence case and zero convergence case with the same effective shear (see also appendix 2). In case of point mass lens model, $\vec{\beta}$ scaled by a factor of $(1-\kappa)^{0.5}$ from zero convergence case, and the cross section scaled by a factor of $\{(1-\kappa)^{0.5}\}^2 = (1-\kappa)$. However, in case of SIS lens model, $\vec{\beta}$

---

[8]   This factor corresponds to magnification factor due to the lens galaxy itself.

does not alter by the effect of convergence, and the cross section is not affected by convergence. Then, σ_{lens} is proportional to $(1 - \kappa)$ for point mass lens, and shows no dependence on κ for SIS lens. On the other hand, γ dependence is complicated. Particularly, in $\gamma < 1$ regime, asteroid-shape caustics dramatically grows with the increase of γ. Of course, we can take into account such behavior into current estimation, but we simply set σ_{lens} equals to $\pi\theta_{\text{E}}^2$ for point mass lens and $\pi\theta_{\text{SIS}}^2$ for SIS lens. If the readers want to know more detailed values, figure 9 can be the reference for this purpose.

From Klypin et al. (1999), $n(M) \simeq 19(M/10^7 M_\odot)^{-1.92}$ and $n(v) \simeq 9.6 \times 10^3 (v/11 \text{ km s}^{-1})^{-3.75}$ inside 140 kpc radius [9] of the lens galaxy. After we perform the integration in equation 20 and 21, we can obtain

$$\Upsilon = 4.2 \times 10^{-2} \{(1 - \kappa)^2 - \gamma^2\}^{-1} \tag{22}$$

for point mass lens and

$$\Upsilon = 1.2 \times 10^{-2} \{(1 - \kappa)^2 - \gamma^2\}^{-1} \tag{23}$$

for SIS lens. In general, multiple images of gravitationally lensed quasars are magnified by a several or a few tenth factor that is identical to $\{(1 - \kappa)^2 - \gamma^2\}^{-1}$. Therefore, we can conclude that roughly ten percent of multiple images of gravitationally lensed quasars are affected by quasar mesolensing due to substructures.

The above values also depend on the spatial distribution of substructures. If substructures are concentrated within 1 arcsec radius which is typical separation between the center of lens galaxy and multiple quasar images, column number density of substructures should be larger than that we used here, and the optical depth will increase from our results.

6. Discussion

6.1. Comments on density profile of substructures

Here, we mention about density profile of substructures. To calculate gravitational lens effects and expected values, we require density profile for each substructure. Unfortunately, even in the case of high resolution, cosmological N-body simulations for galaxy formation do not have enough mass resolutions for substructures, because an individual mass of a dark matter particle is too large and most of substructures are consists from a small number of dark matter particles (e.g., Klypin et al. 1999). Thus, in this paper, we simply treat density profile of substructures as point mass or singular isothermal sphere. As is well known, properties of gravitational lens phenomena depend on density profile of lens objects, and differences of expected values between these two lens models reflect such dependence.

In general, further multiple images are created when the density slope of lens object is smaller than -1. If NFW universal density profile (Navarro, Frenk & White 1997) holds even in

---

[9]   This correspond to 4.11 arcsec in current situation.

the small objects such as substructures, size of substructures as lens object will be smaller than size of core radius of substructures. Consequently, the density slope of substructures is almost identical to that of core region of NFW-profile, ~ -1. In this case, we cannot find any further multiple images caused by quasar mesolensing, and magnification anomaly can be a unique probe to detect substructures. However, we still not have any evidence that NFW-profile holds in small scale such as substructures observationally and theoretically, and observational search for further multiple images caused by quasar mesolensing must be a good approach to test density profile of substructures. If we find signals relate to further multiple images, that is observational evidence not only for existence of numerous substructures but also substructure has density profile which is different from NFW-profile. On the other hand, even if we fail to find such signals expect magnification anomaly, density profile of substructure should be similar to NFW-profile.

6.2. *Total magnification due to quasar mesolensing*

The cumulative distribution of the total magnification depicted in figure 10 and 11 for point mass lens case and SIS lens case, respectively. These figures are valid both of individual mass (or velocity) lens case and lens mass- (or velocity-) integrated case, because magnification does not include any information about lens mass (or velocity) and its properties are same for same convergence and shear case, even if we integrate over mass (or velocity) distribution of lens objects.

Different from the distributions for the image separation and the time delay, these distributions consist from a few bump (or sharp rise/drop). This feature means that the expected value is clustered around a few location. When the external shear is added to axi-symmetric lens model, asteroid-shape caustics or highly magnified regions appear and such regions extend with increasing the shear value. Existence of caustics dramatically changes the magnification pattern, and the shape of distribution becomes to have two or more bump though only single bump appears in the case of no-shear. This feature is clearly seen in upper panels of figure 10 and 11.

The bump at the high μ_{tot} range corresponds to the distribution that the source is inside caustics. However, γ_{eff} exceeds unity, caustics suddenly change from single asteroid shape to double triangle shape as shown in figure 1. Following this dramatic change of magnification properties, demagnified region that never exist in the case of $\gamma_{\text{eff}} < 1$ will appear, and the distribution widely extend toward $\mu_{\text{tot}} < 1$ direction. This feature can clearly be seen in $\gamma_{\text{eff}} =$ 1.5 in upper panels of figure 10 and 11, again. In both lens model, expected value for the magnification reduced by a several factor. It has been already known that some combination of convergence and shear, particularly in the case of $\gamma_{\text{eff}} > 1$, produces demagnified images. From our estimations, it becomes clear that the existence of substructures in lens galaxy sometime causes strong demagnification in an image of multiple quasars. If we find multiple quasars with
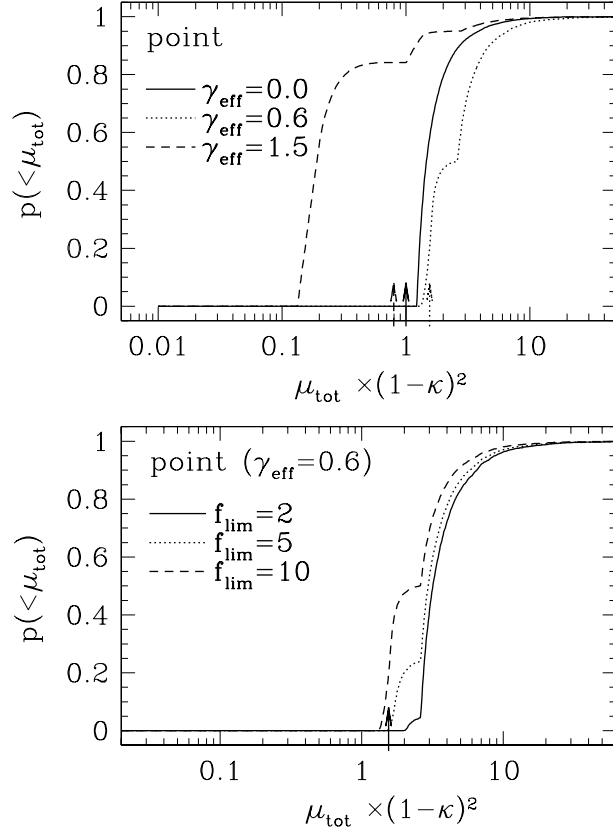
Fig. 10. Cumulative distributions of the total magnification for point mass lens case are presented in this figure. Upper panel shows shear dependence for $f_{lim} = 10$ case. Solid, dotted, and dashed line show $\gamma_{eff} = 0.0$, 0.6, and 1.5 case, respectively. Lower panel shows f_{lim} dependence for $\gamma_{eff} = 0.6$ case. Solid, dotted, and dashed line show $f_{lim} = 2$, 5, and 10 case, respectively. Unit of the abscissa is magnification factor and has no physical dimension. Magnifications caused only by the external shear are denoted by arrows with corresponding line type at the bottom of each panel.

odd number images [10], such systems may be possible candidate for quasars with such strongly demagnified image, and this can be also useful to direct detection for quasar mesolensing and substructures.

Here, we should note that these probability distributions for the total magnification show different properties from that presented by previous researches (e.g., Keeton 2003). The reason is that the distribution in this paper include a condition to take into account observational constraint, f_{lim}, though that in previous researches does not.

For f_{lim} dependence of the total magnification, (lower panels of figure 10 and 11, the reason for the change is explained by the same argument as f_{lim} dependence of image separation in section 4.4. Large f_{lim} means that we can observe fainter image. The more the lens and the source separate, the larger f_{lim} becomes. At the same time, the total magnification becomes small with increase of separation between the lens and the source, because flux of the brightest

---

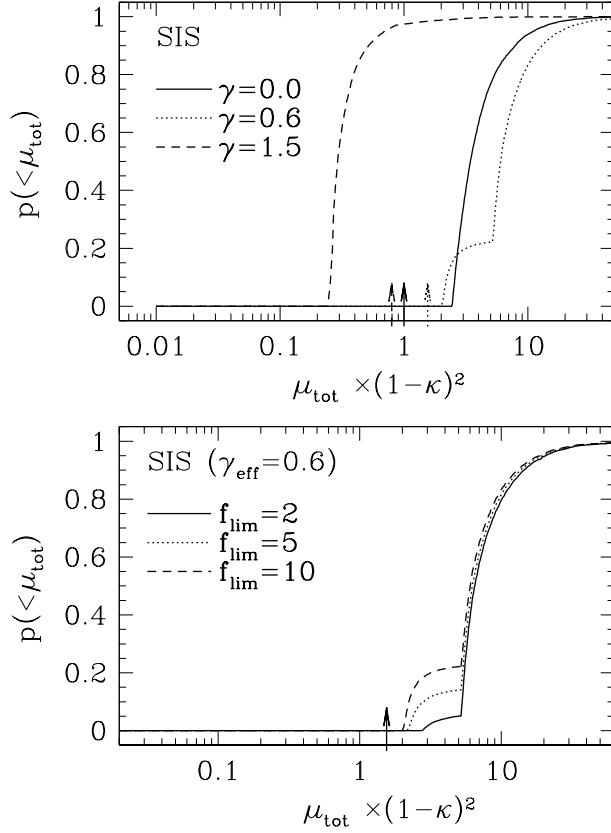[10] Usual multiple quasars have even number images

Fig. 11. Same as figure 10, but for SIS lens case.

image approaches to the original source flux and flux of the secondly brightest image approaches to zero. Therefore, the distribution for large f_{lim} includes such source position case with low magnification (almost unity), and the probability at low μ_{tot} increase. In contrast, the source position at high μ_{tot} is close to the lens and flux of all image is comparable, i.e., f_{lim} is almost unity. Consequently, if we increase f_{lim}, the source position with high magnification may not be newly included. This is the reason why the shape at high μ_{tot} shows no dramatic change. This result indicates that we may easily be able to detect quasar mesolensing signal in multiple quasar with weak magnification anomaly, if we achieve sufficiently high f_{lim} or can detect fainter images.

6.3. Discriminate from quasar microlensing

Further multiple images will be unambiguously detected, if the spatial resolution is sufficiently fine. In contrast, for echo-like flux variation is not so simple. To confirm that the observed, echo-like flux variations are really due to quasar mesolensing, quasar microlensing seems to be somewhat confusing phenomenon. However, the time scale of echo-like flux variations is identical to the time scale of intrinsic quasar variabilities, and the shape of flux variations is also identical to that of intrinsic ones, because gravitational lens effect does not alter the time scale and the shape of flux variations, in principle. Only the difference between

23

echo-like flux variations and intrinsic ones is the flux caused by a magnification factor differ-ence. Moreover, the time scale of quasar microlensing is event time scales of microlensing event, and basically different from that of echo-like flux variations. Then, if we monitor all image of multiple quasars, we can easily obtain intrinsic flux variations of quasars at least from one of the images, because probability that all image suffers quasar mesolensing is less than one percent from previous estimates (section 5.2).

Additionally, echo-like flux variations due to quasar mesolensing occur recurrently during a reasonable epoch, whereas quasar microlensing events occur occasionally. Time scale for quasar microlensing in usual system is expected to be a few year (Wambsganss, Paczyński, & Schneider 1990). In contrast, duration of quasar mesolensing is roughly estimated to be $\sim \theta_{E} D_{ol}/V_{sub}$, where V_{sub} is velocity of motion of substructures around galaxy. If we adopt $10^7 M_{\odot}$ substructure and 200 km s^{-1} for V_{sub}, the time scale becomes 5×10^{12} s $\sim 1.6 \times 10^5$ yr. Duration of quasar mesolensing is sufficiently large compared with our life time, and we can treat quasar mesolensing as static gravitational lensing event. From this argument, echo-like flux variations due to quasar mesolensing is recurrent event, and the echo-like flux variations occur every time when the background quasars show their intrinsic flux variations. This property makes us easier to detect echo-like flux variation and substructures via quasar mesolensing.

6.4. *Toward actual observation*

Quasar mesolensing occurs in ~ 10 % of images in multiple quasars, and we will be able to hunt such further multiple images as a direct evidence for substructures by using observational missions/facilities with $1 \sim 30$ mas spatial resolution or $1 \sim 10^3$ s time resolution. These expected values are not identical in different systems and images, because external convergence and shear due to the lens galaxy are different from system to system and from image to image. Therefore, to estimate the expected values more accurately in an individual system, we have to obtain κ and γ of images via modeling of the lens galaxy. Subsequently, calculate probability distributions for the observables as we shown in this paper. By comparing such probability distribution and observational results, we may be able to discuss about existence and nature of substructures.

To find further multiple images caused by quasar mesolensing directly, we require ob-servational facility with ≤ 30 mas-level spatial resolution. There is also non-zero probability to realize further multiple images with the separation ≥ 30 mas. Unfortunately, flux ratio of such image pairs is large, and the fainter image can be too faint to be detected feasibly. Thus, we really require ≤ 30 mas spatial resolution to detect quasar mesolensing. If we observe images with spatial resolution further below this value, we will clearly detect that the image is consisted by two or more images, and this can be the evidence for the existence of substructures. Even if we perform observation with marginal spatial resolution, we will find one or more structure is attached around the image, and this can be also the evidence for substructures. Simple way to

achieve high spatial resolution is to use interferometers, but it may be practically difficult. The reason is that the light from multiple quasars images pass inside the lens galaxy, and the light suffers the effect such as scintillation due to relatively dense inter stellar medium. Therefore, not interferometric but direct observation is necessary and forthcoming observational instruments such as XMAS (Kitamoto et al. 2003) [11] will be required.

Another solution to find signal due to further multiple images is to hunt echo-like flux variations with $\leq 10^3$ s delay. In this case, high spatial resolution is not required any more, but high time resolution or high speed monitoring is required. Observations of quasars that show rapid and large flare-like flux variations are preferable to search echo-like signal. Generally, quasars always show stochastic flux variations, and it is practically difficult to find out echo-like flux variations due to quasar mesolensing of small flares with long duration. In contrast, large flares with short duration can be clearly detected from stochastic flux variations of quasars, and we can easily pick up corresponding echo-like flux variations due to quasar mesolensing. Considering this point, for example, observation of rapid X-ray flares with time scale of ks (e.g., Chartas et al. 2001) that have recently detected in multiple quasars can be one of the best target. Furthermore, owing to shortness of the time delay, echo-like flux variation may be found by single observation with X-ray satellite. Duration of single observation with X-ray satellite is usually a several tenth of ks, and sufficiently longer than expected time delay estimated in this paper. Thus, if we can detect such rapid X-ray flare and a substructure fortunately located in the vicinity of the image , we will be able to prove the existence of substructures by only single observation. In the situation we are considering here, target quasar has multiple image, and we can discriminate echo-like flux variation due to quasar mesolensing from stochastic intrinsic flux variations in quasars by comparing flux variations in other images. For this confirmation purpose, multiple quasars with less than a day time delay between images are the ideal targets, because corresponding flux variations of delayed image also be able to observed by a single observation and other confusing phenomena such as quasar microlensing can be easily rejected.

A rapid X-ray flare detected in RX J0911.4+0511 by Chartas et al. (2001) corresponds to ~ 15 counts s^{-1} in CHANDRA. To detect echo-like flux variation with $3-\sigma$ confidence level, more than 9 photons for a fainter image are required within a time bin. This $3-\sigma$ detection limits is almost comparable to $f_{\lim} = 15/9 \sim 2$ constraint. Referring figure 6, $f_{\lim} = 2$ constraint reduces expected time delay by a several factor from $f_{\lim} = 10$ constraint that we have applied to calculate figure 7. Even in this case, probability for 10^3 s delay is non-zero, and we will be able to detect echo-like flux variations by using CHANDRA capability. For actual observation, it is better to perform such observation to multiple quasars with magnification anomaly than blind search, because magnification anomaly occurs also in this quasar mesolensing and such multiple quasars may have systematically high probability to show echo-like flux variation caused by quasar mesolensing than usual multiple quasars. The above discussion is limited

---

[11]   This will achieve 3 mas spatial resolution in X-ray.

on a case with $\sim 10^3$ s time delay. If there is no X-ray flares with larger amplitude than that Chartas et al. (2001) have detected, we will have to wait X-ray facility with large collecting area such as XEUS [12] or choose waveband with large signal-to-noise ratio for flares to find the evidence of substructures clearly and strongly. Expected time delay with shorter than $\sim 10^3$ s has significant fraction in cumulative distribution of the time delay as apparently shown in figure 7 and 8, and observational facilities with large collecting area or waveband that realize high signal-to-noise ratio will open a window to detect shorter time delay events.

Until now, phenomena that we are investigated here are not detected, but some coordinated future observations enable us to reveal the existence of substructures around galaxies if CDM scenario for structure formation is totally correct.

---

[12] `http://astro.esa.int/SA-general/Projects/XEUS/`

Appendix 1.   Dependence on Typical Lens Size

Here, we consider the case when the lens size is multiplied by a factor $\mathcal{G}$ and derive scaling law of image separation and time delay between images.

A.1.1.   Point mass lens

We put $\mathcal{G}\vec{\theta'}$ and $\mathcal{G}\vec{\beta'}$ instead of $\vec{\theta}$ and $\vec{\beta}$, respectively, the lens equation becomes

$$\mathcal{G}\vec{\beta'} = (1-\kappa)\mathcal{G}\vec{\theta'} - \gamma(\mathcal{G}\theta'_x, -\mathcal{G}\theta'_y) - \left(\frac{\mathcal{G}\theta_{\rm E}}{|\mathcal{G}\theta'|}\right)^2 \mathcal{G}\vec{\theta'}. \tag{A1}$$

If we divide both side of the equation by $\mathcal{G}$, it reduce to

$$\vec{\beta'} = (1-\kappa)\vec{\theta'} - \gamma(\theta'_x, -\theta'_y) - \left(\frac{\theta_{\rm E}}{|\theta'|}\right)^2 \vec{\theta'}, \tag{A2}$$

and this equation is apparently the same form as the lens equation in the case of point mass lens for $\theta_{\rm E}$. Thus, image separation between multiple images becomes $\vec{\theta_1} - \vec{\theta_2} = \mathcal{G}\left(\vec{\theta'_1} - \vec{\theta'_2}\right)$ and is scaled simply by a factor of $\mathcal{G}$ compared with the case of $\theta_{\rm E}$.

For arrival time delay, the equation becomes following,

$$\Delta t' = \frac{1+z_1}{2}\frac{1}{c}\frac{D_{\rm ol}D_{\rm os}}{D_{\rm ls}}\left[\left(\mathcal{G}\vec{\theta'} - \mathcal{G}\vec{\beta'}\right)^2 - \kappa\left|\mathcal{G}\vec{\theta'}\right|^2 \gamma\{(\mathcal{G}\theta'_x)^2 - \left(\mathcal{G}\theta'_y\right)^2\} - 2\mathcal{G}^2\theta'_{\rm E}\ln\left|\mathcal{G}\vec{\theta'}\right|\right]. \tag{A3}$$

All the term in the right hand side scaled by a factor of $\mathcal{G}^2$ except the last term. Fortunately, the observable is not arrival time delay but time delay between multiple images, $\tau_{1,2}$, and $\mathcal{G}$ inside ln in the last term vanishes when we subtract $\Delta t(\theta'_2)$ from $\Delta t(\theta'_1)$. Thus, the time delay between multiple images is scaled simply by a factor of $\mathcal{G}^2$ compared with the case of $\theta_{\rm E}$, i.e., $\tau'_{1,2} = \mathcal{G}^2 \tau_{1,2}$.

The magnification factor for one image (μ) is calculated from Jacobian matrix for $\vec{\beta} \to \vec{\theta}$ transformation, and written as

$$\mu = \left|\frac{\partial\vec{\beta}}{\partial\vec{\theta}}\right|^{-1} = \left|\frac{\mathcal{G}}{\mathcal{G}}\frac{\partial\vec{\beta'}}{\partial\vec{\theta'}}\right|^{-1} = \left|\frac{\partial\vec{\beta'}}{\partial\vec{\theta'}}\right|^{-1}. \tag{A4}$$

Thus, applying proper re-scaling for $\vec{\theta}$ and $\vec{\beta}$, there is no need to additional scaling for the magnification.

A.1.2.   SIS

Applying the same scaling to $\vec{\beta}$ and $\vec{\theta}$ as the point mass lens, the bending angle ($\vec{\alpha}$) and the lens potential (Ψ) for SIS lens model become

$$\vec{\alpha'} = \frac{\mathcal{G}\theta_{\rm SIS}}{\left|\mathcal{G}\vec{\theta'}\right|}\mathcal{G}\vec{\theta'} \tag{A5}$$

$$= \mathcal{G}\frac{\theta_{\rm SIS}}{\left|\vec{\theta'}\right|}\vec{\theta'} \tag{A6}$$

and

$$\Psi' = \mathcal{G}\theta_{\text{SIS}}\left|\mathcal{G}\vec{\theta'}\right| \tag{A7}$$

$$= \mathcal{G}^2\theta_{\text{SIS}}\left|\vec{\theta'}\right|, \tag{A8}$$

respectively, and the same scaling law as point mass lens case holds also in this case. It is apparent that the scaling law for the magnification properties is same as the case for the point mass lens.

Appendix 2.   Dependence on Convergence

Here, we derive scaling laws for convergence. We consider lens equations and arrival time delays for two cases, non-zero convergence (κ) and shear (γ) case and zero convergence and non-zero shear (γ_{eff}) case. In the latter case, shear is equivalent with the effective shear for the former case, i.e., $\gamma_{\text{eff}} = \gamma/(1-\kappa)$. We set the source position, the image position, arrival time delay, and the magnification factor for non-zero convergence case are β, θ, Δt, and μ, respectively, and that for zero convergence case are β', θ', $\Delta t'$, and μ', respectively.

A.2.1.   Point mass lens

Here, we put θ_{E} as the lens size for non-zero convergence case, and θ'_{E} as the lens size for zero convergence case. In this case, lens equations for both case are written as

$$\vec{\beta} = (1-\kappa)\vec{\theta} - \gamma(\theta_x, -\theta_y) - \left(\frac{\theta_{\text{E}}}{|\vec{\theta}|}\right)^2\vec{\theta},$$

$$\rightarrow \frac{\vec{\beta}}{(1-\kappa)} = \vec{\theta} - \gamma_{\text{eff}}(\theta_x, -\theta_y) - \frac{1}{(1-\kappa)}\left(\frac{\theta_{\text{E}}}{|\vec{\theta}|}\right)^2\vec{\theta}, \tag{A9}$$

$$\vec{\beta'} = \vec{\theta'} - \gamma_{\text{eff}}(\theta'_x, -\theta'_y) - \left(\frac{\theta'_{\text{E}}}{|\vec{\theta'}|}\right)^2\vec{\theta'}. \tag{A10}$$

If we set $\theta'_{\text{E}} = \theta_{\text{E}}/(1-\kappa)^{0.5}$ in equation A9, the lens equation becomes similar form to equation A10. From dependence on lens size presented in appendix 1.1, the source and the image positions of non-zero convergence case should be related to that of zero convergence case as follows,

$$\frac{\vec{\beta}}{(1-\kappa)} = \frac{\vec{\beta'}}{(1-\kappa)^{0.5}} \tag{A11}$$

$$\vec{\theta} = \frac{\vec{\theta'}}{(1-\kappa)^{0.5}}. \tag{A12}$$

The above relation corresponding to scaling law for the source and the image positions between non-zero convergence case and zero convergence with the same effective shear case. Therefore, by using image separation for zero convergence case, $\Delta\theta'_{1,2} = |\vec{\theta'_1} - \vec{\theta'_2}|$, image separation for non-zero convergence case, $\Delta\theta_{1,2} = |\vec{\theta_1} - \vec{\theta_2}|$ is expressed as

$$\Delta\theta_{1,2} = \frac{\Delta\theta'_{1,2}}{(1-\kappa)^{0.5}}. \tag{A13}$$

On the other hand, arrival time delays for both cases are written as

$$\Delta t = \frac{1+z_1}{2}\frac{1}{c}\frac{D_{\mathrm{ol}}D_{\mathrm{os}}}{D_{\mathrm{ls}}}\left[\left(\vec{\theta}-\vec{\beta}\right)^2 - \kappa|\vec{\theta}|^2 - \gamma\left(\theta_x^2 - \theta_y^2\right) - 2\theta_{\mathrm{E}}^2\ln|\vec{\theta}|\right], \tag{A14}$$

$$\Delta t' = \frac{1+z_1}{2}\frac{1}{c}\frac{D_{\mathrm{ol}}D_{\mathrm{os}}}{D_{\mathrm{ls}}}\left[\left(\vec{\theta'}-\vec{\beta'}\right)^2 - \gamma_{\mathrm{eff}}\left(\theta_x'^2 - \theta_y'^2\right) - 2\theta_{\mathrm{E}}'^2\ln|\vec{\theta'}|\right]. \tag{A15}$$

By using equation A11 and A12, equation A14 becomes

$$\Delta t = \frac{1+z_1}{2}\frac{1}{c}\frac{D_{\mathrm{ol}}D_{\mathrm{os}}}{D_{\mathrm{ls}}}\left[\left(\frac{\vec{\theta'}}{(1-\kappa)^{0.5}} - (1-\kappa)^{0.5}\vec{\beta'}\right)^2 - \kappa\frac{|\vec{\theta'}|^2}{(1-\kappa)} - \right.$$
$$\left. \frac{\gamma}{(1-\kappa)}\left(\theta_x'^2 - \theta_y'^2\right) - 2\theta_{\mathrm{E}}^2\left(\ln|\vec{\theta'}| - \ln|1-\kappa|^{0.5}\right)\right], \tag{A16}$$

$$= \frac{1+z_1}{2}\frac{1}{c}\frac{D_{\mathrm{ol}}D_{\mathrm{os}}}{D_{\mathrm{ls}}}\left[\left(\vec{\theta'}-\vec{\beta'}\right)^2 - \gamma_{\mathrm{eff}}\left(\theta_x'^2 - \theta_y'^2\right) - 2\theta_{\mathrm{E}}^2\ln|\vec{\theta'}|\right.$$
$$\left. -\kappa|\vec{\beta'}| + \theta_{\mathrm{E}}^2\ln|1-\kappa|\right]. \tag{A17}$$

Comparing with equation A15, equation A17 has 4-th and 5-th terms in the parenthesis as extra terms. Fortunately, observable is not arrival time delay but arrival time delay difference between images, $\tau_{1,2} = \Delta t_1 - \Delta t_2$. These extra terms are constant and they cancel out in time delay between images. Therefore, time delay between images in the case of non-zero convergence, $\tau_{1,2}$, and that in the case of zero convergence with the same effective shear, $\tau'_{1,2}$ are related as follows,

$$\tau_{1,2} = \tau'_{1,2}. \tag{A18}$$

After this transformation, we can easily calculate scaling law for the magnification factor, μ. As same as the lens size dependence, μ is expressed as

$$\mu = \left|\frac{\partial\vec{\beta}}{\partial\vec{\theta}}\right|^{-1} = \left|\left(\frac{(1-\kappa)^{0.5}}{(1-\kappa)^{-0.5}}\right)^2\frac{\partial\vec{\beta'}}{\partial\vec{\theta'}}\right|^{-1} = \frac{1}{(1-\kappa)^2}\left|\frac{\partial\vec{\beta'}}{\partial\vec{\theta'}}\right|^{-1} = \frac{1}{(1-\kappa)^2}\mu'. \tag{A19}$$

Thus, if we want to obtain the magnification factor for non-zero convergence case, μ, we will only multiply by a factor of $(1-\kappa)^{-2}$ to the magnification factor for zero convergence case, μ'. All image is multiplied by the same factor, $(1-\kappa)^{-2}$, and magnification ratio between two images does not alter in this transformation.

A.2.2. SIS

If we put θ_{SIS} as the lens size for non-zero convergence case, θ'_{SIS} as the lens size for zero convergence case, and apply bending angle and lens potential for SIS lens model, we can lead scaling relation for convergence in the case of SIS lens model as same as the case of point mass lens.

The form of bending angle and lens potential is different from the point mass lens case, κ dependence of SIS lens case is different from the point mass lens case. Comparing lens equation for non-zero convergence case and that for zero convergence case, both lens equation will become similar form, if we set $\theta'_{\mathrm{SIS}} = \theta_{\mathrm{SIS}}/(1-\kappa)$. Consequently, scaling law for the source and the image position become followings,

$$\frac{\vec{\beta}}{(1-\kappa)} = \frac{\vec{\beta'}}{(1-\kappa)}, \tag{A20}$$

$$\vec{\theta} = \frac{\vec{\theta'}}{(1-\kappa)}. \tag{A21}$$

Therefore, relation between image separation for non-zero convergence case and that for zero convergence case is expressed as

$$\Delta\theta_{1,2} = \frac{\Delta\theta'_{1,2}}{(1-\kappa)}. \tag{A22}$$

Moreover, for arrival time delay, if we perform similar derivation to the case of point mass lens, relation between time delay between images for non-zero convergence case and that for zero convergence case is presented as

$$\tau_{1,2} = \frac{\tau'_{1,2}}{(1-\kappa)}. \tag{A23}$$

Again, scaling law for magnification factor is same as in the case of point mass lens, and magnification ratio between two images is identical when the effective shear is same.

References

Chang, K., & Refsdal, S. 1984, A&A, 132, 168

Chartas, G., Dai, X., Gallagher, S.C., Garmire, G.P., Bautz, M.W., Schechter, P.L., & Morgan, N.D. 2001, ApJ, 558, 119

Chiba, M. 2002, ApJ, 565, 17

Dalal, N., & Kochanek, C.S. 2002, ApJ, 572, 25

Falco, E.E., Gorenstein, M.V., & Shapiro, I.I. 1985, ApJ, 289, 1

Gil-Merino, R., Wisotzki, L., & Wambsganss, J. 2002, A&A, 381, 428

Jackson, N.J., Xanthopoulos, E., & Browne, I.W.A. 2000, MNRAS, 311, 389

Keeton, C.R. 2001, submitted to ApJ(astro-ph/0102340)

Keeton, C.R. 2003, ApJ, 584, 664

Kitamoto, S. et al. 2003, Proceedings of "IAU 8th Asian-Pasific Regional Meeting" volume I, in press

Kitayama, T., Susa, H., Umemura, M., & Ikeuchi, S. 2001, MNRAS, 326, 1353

Klypin, A., Gottlöber, S., Kravtsov, A.V., & Khokhlov, A.M. 1999, ApJ, 516, 530

Lee, M.H. & Spergel, D.N. 1990, ApJ, 357, 23

Mao, S. & Schneider, P. 1998, MNRAS, 295, 587

Metcalf, R.B. 2002, ApJ, 580, 696

Metcalf, R.B., & Madau, P. 2001, ApJ, 563, 9

Metcalf, R.B., & Zhao, H.S. 2002, ApJ, 567, L5

Moore, B., Ghigna, S., Governato, F., Lake, G., Quinn, T., Stadel, J., & Tozzi, P. 1999, ApJ, 524, L19

Navarro, J.F., Frenk, C.S., & White, S.D.M. 1997, ApJ, 490, 493

Nishi, R., & Susa, H. 1999, ApJ, 523, L103

Oshima, T., Mitsuda, K., Ota, N., Yonehara, A., Hattori, M., Mihara, T., & Sekimoto, Y. 2001, ApJ, 551, 929

Østensen, R., et al. 1996, A&A, 309, 59

Østensen, R., et al. 1997, A&AS, 126, 393

Padmanabhan, T. 1993, Structure formation in the universe(Cambridge University Press, Cambridge) page283

Schmidt, R., Webster, R.L., & Lewis, G.F. 1998, MNRAS, 295, 488

Spergel, D.N., et al. 2003, submitted to ApJ(astro-ph/0302209)

Susa, H., & Umemura, M. 2003, in preparations

Wambsganss, J., Paczyński, B., & Schneider, P. 1990, ApJ, 358, L33